

Systematic Study of the Self-Renormalized Nucleon Gluon PDF in Large-Momentum Effective Theory

Alex NieMiera  ^{1, 2, *} William Good  ^{1, 2, †} Huey-Wen Lin  ¹ and Fei Yao  ³

¹*Department of Physics and Astronomy, Michigan State University, East Lansing, Michigan 48824, USA*

²*Department of Computational Mathematics, Science and Engineering,*

Michigan State University, East Lansing, Michigan 48824, USA

³*Physics Department, Brookhaven National Laboratory, Upton, New York 11973, USA*

(Dated: November 19, 2025)

We present a systematic study of the nucleon gluon parton distribution function (PDF) using the self-renormalized large-momentum effective theory (LaMET) approach in lattice QCD. This work extends previous gluon-PDF extractions by performing a detailed analysis of key systematic effects, including gauge-link smearing, lattice spacing, pion mass, and nucleon boost momentum. The self-renormalization framework mitigates ultraviolet divergences associated with Wilson-line self-energy and renormalon contributions by combining lattice matrix elements with perturbative short-distance information, thereby preserving the correct infrared structure. Calculations are performed on $N_f = 2 + 1 + 1$ HISQ ensembles generated by the MILC Collaboration at three lattice spacings and two pion masses, with boosted nucleon states reaching momenta up to 2.2 GeV. We determine renormalization factors from zero-momentum matrix elements and apply hybrid renormalization to suppress discretization artifacts. After extrapolating large-separation behavior and performing Fourier transforms, we reconstruct quasi-PDFs and match them to lightcone PDFs using next-to-leading order Wilson coefficients. Our results demonstrate that smearing and lattice-spacing effects are under control, and pion-mass and lattice-spacing dependence is mild relative to the current $O(10^6)$ statistics; however, momentum dependence remains a significant source of uncertainty. Future work including even larger boost momenta will be essential to reduce systematics in lattice determinations of the gluon PDF and to advance toward precision QCD phenomenology at the LHC and the future Electron-Ion Collider.

I. INTRODUCTION

Parton distribution functions (PDFs) are nonperturbative quantities that encode the momentum distributions of quarks and gluons inside hadrons. They are essential inputs for theoretical predictions of high-energy scattering processes, such as those measured at the Large Hadron Collider (LHC). In particular, uncertainties in the gluon PDF limit the theoretical precision of key processes, including Higgs-boson production, jet production, and heavy-flavor dynamics, which are central to testing the Standard Model and probing potential new physics. While the quark structure of the proton is relatively well constrained by deep inelastic scattering (DIS) and Drell-Yan measurements, these processes are only indirectly sensitive to gluons, especially in the intermediate- and large- x regions. Constraining the gluon PDF in these kinematic domains, therefore, relies on sparser data sets, such as inclusive jet production and top-quark observables [1]. Differences in data cuts and theoretical treatments across global analyses have led to a lack of consensus on the gluon distribution, underscoring the need for improved constraints [2, 3]. Ongoing and future measurements at the LHC, as well as the upcoming Electron-Ion Collider (EIC), are expected to significantly reduce

gluon PDF uncertainties and improve our understanding of proton structure [4–6].

In contrast to global PDF extractions, which rely on phenomenological fits to a wide range of experimental cross sections, lattice QCD provides a systematically improvable, first-principles approach to accessing the nonperturbative structure of hadrons. Over the past decade, significant progress has been made in computing x -dependent parton distributions on the lattice through methods such as large-momentum effective theory (LaMET) [7] and the pseudo-PDF framework [8]. These approaches have enabled determinations of momentum-fractions-dependent shapes for isovector nucleon, valence-pion quark PDFs and generalized parton distributions, as reviewed in Refs. [9–12]. However, lattice calculations of gluon PDFs remain considerably more challenging. The number of available studies is much smaller, and the associated uncertainties are typically larger than for quark distributions. Most existing work has employed the pseudo-PDF method with simplified functional parameterizations for the x dependence of the hadron gluon distribution [13–20]. Only recently have the first extractions of the nucleon gluon PDF using LaMET become feasible, enabled by improved control of the long-distance behavior of the relevant matrix elements [21–23].

In this work, we extend our recent determination of the nucleon gluon parton distribution using the self-renormalized LaMET approach [23] by performing a detailed study of several key systematic effects, including

*Electronic address: niemiera@msu.edu

†Electronic address: goodwil9@msu.edu

gauge-link smearing, lattice spacing, pion mass, and nucleon boost momentum. This represents an important step toward achieving full systematic control in lattice QCD extractions of the gluon PDF using LaMET.

The self-renormalization procedure [24] removes divergences associated with the Wilson-line self-energy, renormalon contributions, and both leading and subleading logarithmic ultraviolet behavior by combining lattice matrix elements with perturbative short-distance information. In doing so, it mitigates lattice-spacing artifacts while preserving the correct infrared structure of the matrix elements, avoiding distortions that can arise in purely nonperturbative renormalization schemes. Until now, this framework has been applied primarily to quark bilinear observables [25–28], and our study marks its first systematic application to the gluon sector. We show that the self-renormalization method provides robust control over smearing- and lattice-spacing-related uncertainties. Additionally, pion mass effects are comparatively mild, while the dependence on the nucleon boost momentum remains one of the leading sources of systematic uncertainty, requiring further refinement in future calculations.

The rest of this paper is organized as follows: in Sec. II we give the lattice details of our calculation, describe self-renormalization of the gluon operator, and show our self-renormalized zero momentum matrix elements. In Sec. III, we explore smearing and lattice spacing effects in our self-renormalized matrix elements, demonstrate the large- ν extrapolations, show the effects of matching, and explore various systematic effects on the PDFs. We conclude and make remarks on future work in Sec. IV.

II. LATTICE DETAILS AND SELF-RENORMALIZATION FACTORS

A. Lattice Details

For this study, we analyze high-statistics measurements on gauge-field ensembles generated by the MILC Collaboration [29], corresponding to lattice spacings of approximately $a \approx 0.15, 0.12$, and 0.09 fm. The ensembles contain $N_f = 2 + 1 + 1$ flavors of highly improved staggered quarks (HISQ) in the sea sector [30], with valence pion masses of $M_\pi \approx 310$ and 690 MeV. In the valence sector, we employ clover-improved Wilson fermions, with the quark masses tuned to match the light and strange quark masses in the HISQ sea. This mixed-action setup follows the strategy extensively used by the PNDME Collaboration in previous precision studies of nucleon structure over multiple lattice spacings and quark masses [31–40]. No evidence of exceptional configurations was observed in either the two-point or three-point correlation functions on any of the ensembles considered in this work.

To determine the self-renormalization factors, we generated approximately $O(10^5)$ two-point correlation functions for the η_s meson at zero momentum. For the

nucleon matrix elements relevant to the PDF extractions, we computed $O(10^6)$ two-point correlators at both the light and heavy pion masses, employing Gaussian momentum smearing to improve overlap with boosted states [41]. The η_s correlators were constructed using the $\bar{s}\gamma_t\gamma_5s$ interpolating operator, while the nucleon interpolating operator was taken as $\epsilon_{abc}(d_a^T C \gamma_5 u_b) \mathcal{P} + u_c$, where C denotes the charge-conjugation matrix and $\mathcal{P}+$ projects onto positive-parity states. Although alternative high-momentum-optimized operator constructions have recently been proposed in Ref. [42], much of the correlator data used in this analysis was produced prior to their introduction. Additionally, the improvement associated with these newer operators scales inversely with the hadron mass, and thus is expected to be less pronounced for the heavier-than-physical pion masses considered here. Details of the lattice ensembles and simulation parameters are provided in Table I. For convenience, we refer to the nucleon states obtained at the lighter and heavier pion masses as N_l and N_s , respectively. Following the methodology used in the MSULat program [13, 14, 18–22], two- and three-point correlation functions are analyzed using simultaneous two-state fits, with the fit windows optimized to suppress excited-state contamination.

Previous lattice studies have demonstrated that reliable signals for gluon correlators typically require the use of gauge-link smearing [13–22, 43, 44]. In contrast, the analytical formulation of self-renormalization is derived for unsmeared Wilson lines, although it has been shown that the method remains valid as long as the smearing radius is sufficiently small compared with the inverse boost momentum [45]. Because a fully established framework for incorporating smearing into self-renormalization is not yet available, we take this opportunity to assess the impact of different smearing prescriptions by performing three complementary analyses, each employing a different choice of Wilson flow [46] in the construction of the gluon operators.

Wilson flow is characterized by a flow time $\mathcal{T}_W = twa^2$, where tw is a dimensionless parameter and a is the lattice spacing. Our first analysis uses a uniform relative smearing choice with $tw = 3$ for all ensembles. This corresponds to physical flow times ranging from $\mathcal{T}_W \approx 0.024$ fm 2 on the finest lattice to $\mathcal{T}_W \approx 0.068$ fm 2 on the coarsest lattice, resulting in approximately constant smearing in lattice units. We refer to this approach as the fixed relative smearing method. To contrast with this, we also examine two fixed physical smearing schemes, in which we select flow times to maintain approximately constant \mathcal{T}_W across lattice spacings. Specifically, we employ $tw = \{1, 2, 3\}$ on the coarsest ensemble and $tw = \{2, 3, 5\}$ on the finest one, which correspond to physical flow-time ranges of $\mathcal{T}_W \approx 0.023$ – 0.029 fm 2 and $\mathcal{T}_W \approx 0.040$ – 0.046 fm 2 , respectively. For convenience, we label these three analyses as W333 (fixed relative smearing), W123, and W235 (fixed physical smearing), and use this notation throughout the remainder of the paper.

Ensemble	a09m310	a12m310	a15m310
a (fm)	0.0888(8)	0.1207(11)	0.1510(20)
$L^3 \times T$	$32^3 \times 96$	$24^3 \times 64$	$16^3 \times 48$
M_π^{val} (GeV)	0.313(1)	0.309(1)	0.319(3)
$M_{\eta_s}^{\text{val}}$ (GeV)	0.698(7)	0.6841(6)	0.687(1)
P_z (GeV)	{0, 1.31, 1.75, 2.18}	{0, 1.28, 1.71, 2.14}	{0, 1.54, 2.05, 2.57}
N_{cfg}	1026	1013	900
$N_{\text{meas}}^{\text{2pt}} (P_z = 0)$	196,992	64,832	129,600
$N_{\text{meas}}^{\text{2pt}} (P_z \neq 0)$	1,378,944	1,555,968	950,400

TABLE I: For each HISQ ensemble generated by the MILC Collaboration and used in this analysis, we list the lattice spacing a , lattice volume $L^3 \times T$, the valence pion mass M_π^{val} , the valence η_s mass $M_{\eta_s}^{\text{val}}$, and the values of the hadron momenta P_z employed. We also provide the number of gauge configurations N_{cfg} analyzed, together with the number of two-point correlator measurements performed at zero momentum, $N_{\text{meas}}^{\text{2pt}}(P_z = 0)$, and at nonzero momentum, $N_{\text{meas}}^{\text{2pt}}(P_z \neq 0)$.

In the W333 analysis, a fixed relative smearing is used, for which $\mathcal{T}_W = t_W a^2$ scales with a^2 and the smoothing scale $1/\sqrt{8\mathcal{T}_W}$ remains proportional to $1/a$, preserving the standard $1/a$ linear divergence and ensuring the validity of the self-renormalization formula. For W123 and W235, we instead employ fixed-physical smearing, where \mathcal{T}_W is approximately constant across lattice spacings; although the linear divergence no longer scales as $1/a$, the resulting modulation can be absorbed into the renormalon term m_0 and the nonperturbative function $g(z)$ in our parameterization, leaving the multiplicative state-independent UV structure intact and allowing the same self-renormalization relation to be used.

B. Self-Renormalization Factor Determination

In the LaMET framework, we begin with the bare spatially separated matrix elements,

$$\tilde{h}^B(z, P_z, 1/a) = \langle P | O(z) | P \rangle, \quad (1)$$

where $|P\rangle$ denotes a hadron state boosted to momentum P_z , and $O(z)$ is a gauge-invariant nonlocal gluon operator with separation z . Although several multiplicatively renormalizable gluon operators can, in principle, be used to access the gluon PDF [8, 47], we find that the operator introduced in Ref. [8] provides the most reliable signal for extracting renormalized matrix elements. This operator is defined as

$$O(z) = F^{ti}(z) U(z, 0) F_i^t(0) - F^{ij}(z) U(z, 0) F_{ij}(0), \quad (2)$$

where the indices i, j denote the transverse directions $\{x, y\}$, and $U(z, 0)$ is a Wilson line that ensures gauge invariance. The gluon field-strength tensor is given by

$$F_a^{\mu\nu} = \partial^\mu A_a^\nu - \partial^\nu A_a^\mu - g f_{abc} A_b^\mu A_c^\nu. \quad (3)$$

To remove the ultraviolet (UV) divergences present in the bare quasi-correlation function $\tilde{h}^B(z, P_z, 1/a)$, one introduces a multiplicative renormalization factor [47]:

$$\tilde{h}^B(z, P_z, 1/a) = Z_L(a) e^{-\delta m(a)|z|} \tilde{h}^R(z, P_z), \quad (4)$$

where \tilde{h}^R denotes the renormalized matrix element. The function $Z_L(a)$ cancels the logarithmic divergences that do not depend on the Wilson-line length z , while the exponential factor containing $\delta m(a)$ removes the Wilson-line self-energy divergence that grows linearly with z . Fully nonperturbative renormalization prescriptions [48–53], however, typically suffer from undesirable nonperturbative artifacts introduced by the renormalization factor itself, which can alter the infrared behavior of the quasi-correlation function. The hybrid renormalization approach [54] mitigates this issue by treating short- and long-distance contributions separately. In this scheme, the renormalized correlation is defined as

$$\begin{aligned} \tilde{h}^R(z, P_z) &= \frac{\tilde{h}^B(z, P_z, 1/a)}{\tilde{h}^B(z, P_z = 0, 1/a)} \theta(z_s - |z|) \\ &\quad + T_s \frac{\tilde{h}^B(z, P_z, 1/a)}{Z_R(z, 1/a)} \theta(|z| - z_s), \end{aligned} \quad (5)$$

where z_s specifies the separation between the short- and long-distance regions, and T_s is a matching factor chosen to ensure smooth behavior at $|z| = z_s$. For $|z| < z_s$, the ratio method [51] is employed to remove the z -dependent UV divergences associated with the Wilson line. For $|z| > z_s$, we instead apply a self-renormalization procedure in which $Z_R(z, 1/a)$ is obtained from a global fit of zero-momentum matrix elements evaluated at multiple lattice spacings.

To carry out self-renormalization, we compute the renormalization factors using matrix elements evaluated in the hadron rest frame. The bare matrix element at zero momentum, $\tilde{h}^B(z, P_z = 0, 1/a)$, is connected to the corresponding renormalized matrix element $\tilde{h}^R(z, P_z = 0)$ via a multiplicative renormalization factor:

$$\tilde{h}^B(z, P_z = 0, 1/a) = Z_R(z, 1/a) \tilde{h}^R(z, P_z = 0). \quad (6)$$

The factor $Z_R(z, 1/a)$ is computed at one-loop order within the operator-product-expansion framework and depends explicitly on the operator under consideration.

Its functional form can be expressed as

$$Z_R(z, 1/a) = \exp \left[\frac{kz}{a \ln(a \Lambda_{\text{QCD}})} + m_0 z + f(z) a^2 + \frac{5C_A}{3b_0} \ln \left(\frac{\ln[1/(a \Lambda_{\text{QCD}})]}{\ln[\mu/\Lambda_{\text{QCD}}]} \right) + \ln \left(1 + \frac{d}{\ln(a \Lambda_{\text{QCD}})} \right) \right]. \quad (7)$$

In this expression, the first term represents a linear divergence in the lattice spacing, the $m_0 z$ term encodes finite mass contributions arising from renormalization ambiguities, and $f(z)a^2$ parametrizes discretization effects associated with the lattice action. The final two terms account for the resummation of leading and sub-leading logarithmic divergences.

In the $\overline{\text{MS}}$ scheme, the next-to-leading order (NLO) Wilson coefficient for the gluon is given by [22]:

$$C_{0,\text{NLO}}(z, \mu) = 1 + \frac{\alpha_s(\mu)C_A}{4\pi} \left[\frac{5}{3} \ln \left(\frac{z^2 \mu^2}{4e^{-2\gamma_E}} \right) + 3 \right], \quad (8)$$

where γ_E denotes the Euler-Mascheroni constant. To extract the parameters in Eq. 7, we adopt the methodology of Ref. [55] and perform a global fit using the ansatz

$$\ln \tilde{h}^B(z, P_z = 0, 1/a) = \ln [Z_R(z, 1/a)] + \begin{cases} \ln[C_{0,\text{NLO}}(z, \mu)], & z_0 \leq z \leq z_1, \\ g(z) - m_0 z, & z > z_1, \end{cases} \quad (9)$$

treating k , Λ_{QCD} , $f(z)$, d , m_0 , and $g(z)$ as free parameters. The fit is applied to interpolated zero-momentum η_s matrix elements at lattice spacings $a \approx 0.09$, 0.12 , and 0.15 fm. We use η_s as the external state since the renormalization factors should be state-independent.

Our previous LaMET study [22] verified that both the linear divergence and the renormalon ambiguity are statistically consistent across different hadron states for a single lattice spacing. Here, we consider three smearing setups, W123, W234, and W333, with $z_0 = 0.05$ fm and $z_1 = 0.36$ fm, fixing the renormalization scale at $\mu = 2$ GeV. A more detailed investigation of the scale dependence is deferred to future work. The fitted parameters and the corresponding χ^2/dof for each global fit are summarized in Table II. All χ^2/dof values are close to unity, indicating that each fit is equally reliable.

For the W333 case, the physical interpretation of individual parameters should be treated with caution, as quantities such as the linear divergence are expected to depend on the smearing radius. In contrast, for W123 and W235, we observe that both the linear divergence k and the renormalon parameter m_0 are larger for smaller smearing radii, consistent with the expectation that increased smearing reduces the decay rate of the correlators, effectively lowering the sum of k and m_0 . The parameter d is statistically consistent with zero across all

Parameter	W123	W235	W333
k	1.02(52)	0.660(27)	0.633(26)
d	$-2.22(13) \times 10^{-13}$	$-1.23(53) \times 10^{-14}$	-0.0008(78)
Λ_{QCD} (GeV)	0.133(54)	0.140(52)	0.264(77)
m_0 (GeV)	0.39(43)	0.099(20)	0.13(25)
χ^2/dof	1.04(96)	0.89(71)	0.81(62)

TABLE II: A summary of the fitted parameters and the corresponding goodness of fit (χ^2/dof) from the global fit to Eq. 9 is also provided.

three analyses, suggesting limited sensitivity to subleading logarithmic effects at the current statistical precision. The extracted Λ_{QCD} values lie within reasonable ranges of 150–300 MeV. Finally, we note that the fit parameters are strongly correlated, such that large standard deviations do not necessarily indicate poor control over the fits, a feature also highlighted in the original self-renormalization study [45], which demonstrates extended valleys of acceptable χ^2/dof among correlated parameters.

We further compare the renormalized zero-momentum values with the perturbative Wilson coefficient given in Eq. 8 for the three analyses, as shown in Fig. 1. At short distances, the matrix elements exhibit reasonable agreement with the perturbative Wilson coefficients, as expected, while noticeable deviations emerge at larger distances. All three analyses display similar qualitative trends; however, the W123 analysis appears to follow perturbation theory over a somewhat wider range than the other two cases with greater smearing. This difference may stem from the relatively larger statistical fluctuations in the latter analyses. Among the three, the W235 analysis yields the smallest uncertainties, likely due to the enhanced smearing applied to the finest lattice spacing.

III. LAMET NUMERICAL RESULTS

With the renormalization factor determined, we examine how the different smearing prescriptions influence the resulting matrix elements. Fig. 2 displays the renormalized results at three nonzero momenta for the ensembles with $M_\pi \approx 690$ MeV. This heavier pion mass is chosen because it typically yields reduced statistical fluctuations. The hybrid-renormalization reference scale is fixed to $z_s = 0.36$ fm, as indicated in Eq. 5. Beginning with the $a \approx 0.09$ fm ensemble (upper panel in Fig. 2), we compare W123 (circles) and W333 (crosses), which differ by whether the smearing is held fixed in physical or relative units during the self-renormalization procedure, while maintaining the same Wilson-line smearing of $\mathcal{T}_W = 3a^2$ on this ensemble. The resulting matrix elements show excellent statistical agreement: both central values and uncertainties coincide over all values of

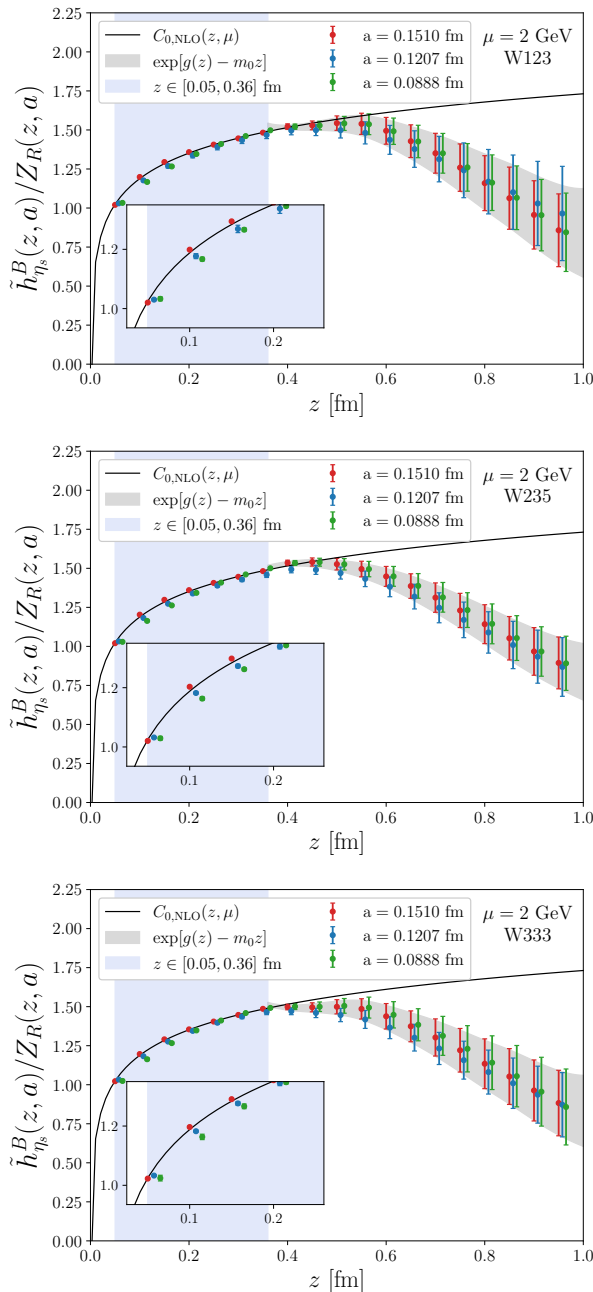


FIG. 1: The renormalized matrix elements for analyses (top) W123, (middle) W235, and (bottom) W333 compared to the perturbative one-loop MS result illustrated by the black curve.

z and P_z . The W235 analysis (diamonds), which employs a slightly larger total smearing $\mathcal{T}_W = 5a^2$, exhibits marginally reduced statistical uncertainties, while remaining consistent within one standard deviation of the other two determinations.

A similar comparison is seen for the $a \approx 0.12$ fm ensemble (middle panel in Fig. 2). Here, W235 and W333 again share $\mathcal{T}_W = 3a^2$ but differ in whether the smearing is fixed in physical or relative units for renormaliza-

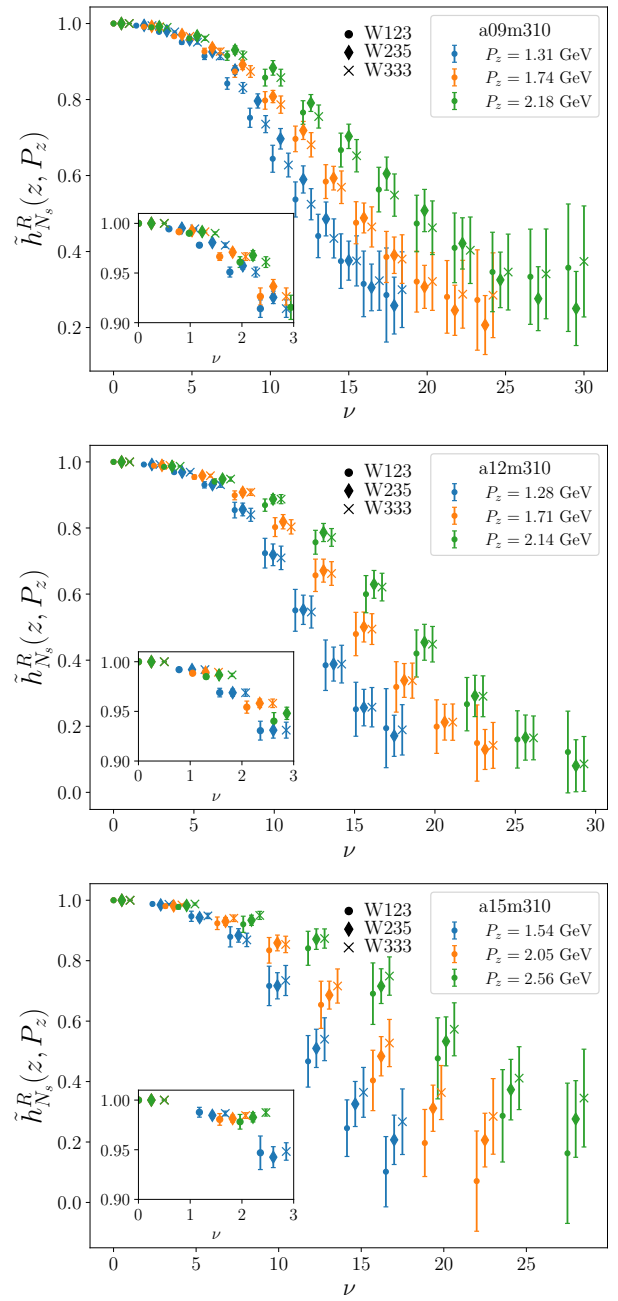


FIG. 2: The renormalized gluon matrix elements at $M_\pi \approx 690$ MeV are compared across the three smearing schemes at three boosted momenta P_z and lattice spacings $a \approx 0.09$ fm (top), 0.12 fm (middle), and 0.15 fm (bottom).

tion, whereas W123 uses a distinct smearing level. The central values remain closely aligned, though the uncertainties appear slightly reduced when the renormalization incorporates the additional statistical stabilizing effects observed at $a \approx 0.09$ fm. The W123 results remain fully consistent with the other two analyses. Finally, the $a \approx 0.15$ fm results (bottom panel in Fig. 2) show agreement among all three analyses within statistical uncer-

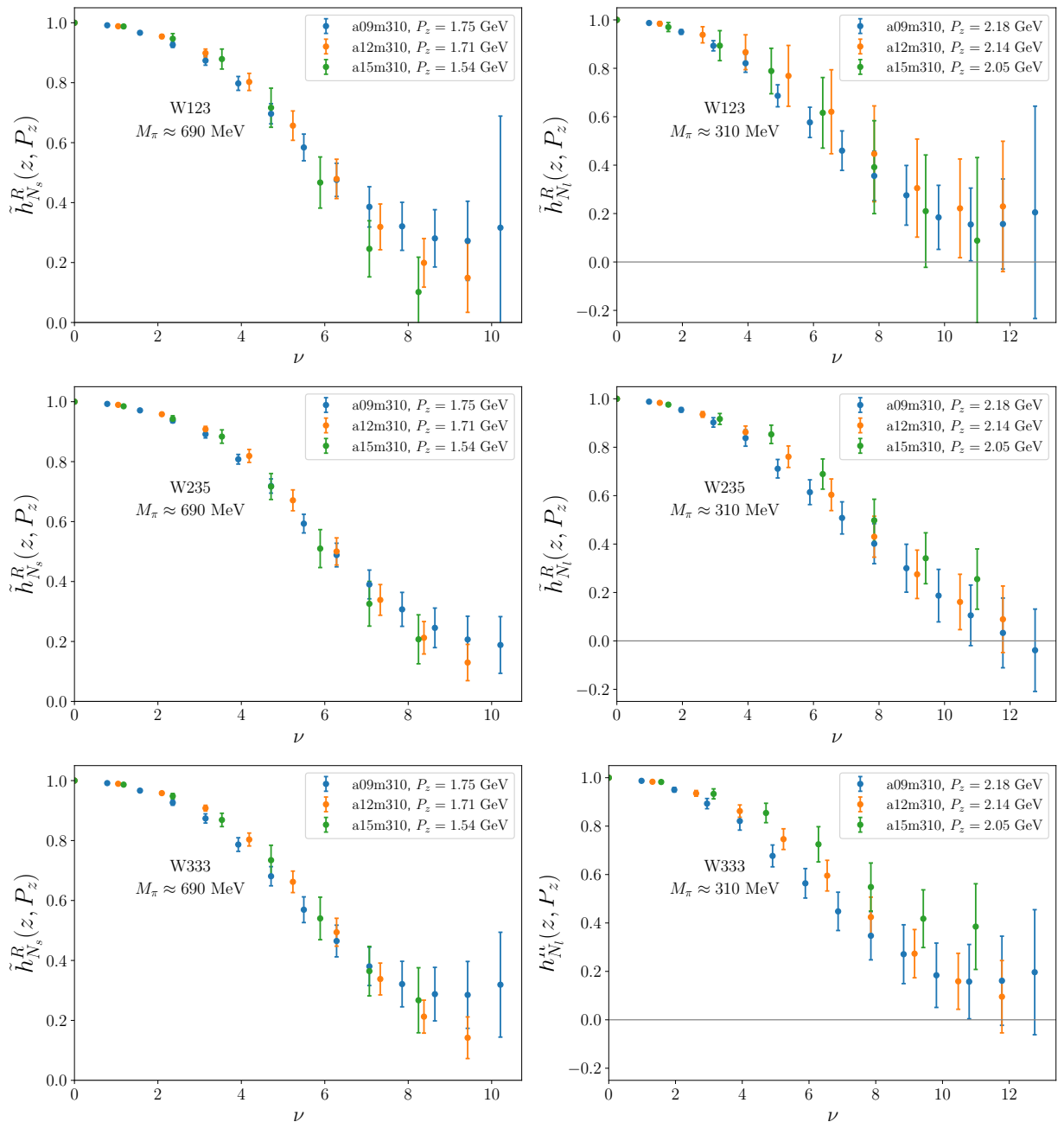


FIG. 3: Renormalized matrix elements compared across each of the three lattice spacings $a \approx 0.09, 0.12, 0.15$ three smearing analyses at $M_\pi \approx 690$ (left column) and 310 (right column) MeV for each of the three analyses W123 (top row), W235 (middle row), and W333 (bottom row).

tainties. While the W235 smearing is smaller than that of W333 on this ensemble, the uncertainties for W235 are modestly reduced in several cases, which may again reflect the constraint introduced by the finer-lattice renormalization input.

A central purpose of the self-renormalization procedure is to suppress the dependence of the renormalized matrix elements on the lattice spacing. In Fig. 3, we present the renormalized nucleon matrix elements for two representa-

tive momenta at both the heavier (left) and lighter (right) pion masses, evaluated on the three lattice spacings and for all three smearing analyses. Across these results, the residual lattice-spacing effects are generally mild, with the data typically agreeing within one to two standard deviations. The most noticeable deviations occur for the W333 ensemble at the lighter pion mass (bottom-right panel), where points around $\nu \approx 4-5$ lie slightly outside the two-standard-deviation band. This may indicate a

somewhat stronger interplay of smearing and discretization artifacts at lower pion mass, but such effects can be systematically addressed through a controlled continuum extrapolation.

Taken together, the three preceding figures suggest that, at the present statistical precision, the choice of smearing has only a modest impact on the extracted matrix elements. More significantly, the self-renormalization approach appears robust for both fixed-physical and fixed-relative smearing conditions. This is consistent with the expected scaling of the linear divergence, which is modulated by a factor proportional to $1/\sqrt{T_W}$ [56]. For fixed relative flow time, one has $1/\sqrt{T_W} \propto 1/a$, so that the corresponding linear divergence is effectively absorbed into the leading term of Eq. 7. Conversely, when the physical flow time is held fixed, the modulation can be accommodated through the renormalon term m_0 , together with the nonperturbative function $g(z)$ in the parameterization. We note that the self-renormalization framework was not originally developed with smeared operators in mind, and a more detailed investigation of this behavior will be pursued in future work.

To reconstruct the lightcone PDF, we first obtain the quasi-PDF in momentum space by performing a Fourier transformation of the renormalized spatial correlation function. The quasi-PDF is then matched to the lightcone PDF using the appropriate perturbative matching kernel. Since the Fourier transform is sensitive to the long-distance behavior of the matrix elements, a reliable description of the correlation function at separations larger than those directly accessible on the lattice is required to mitigate unphysical oscillatory artifacts in the quasi-PDF.

Following Ref. [54], we adopt the extrapolation form

$$h^R(z, P_z) \approx A \frac{e^{-m\nu}}{|\nu|^d}, \quad (10)$$

where $\nu = zP_z$ and A , m , and d are fit parameters. This functional form is motivated by theoretical considerations discussed in Ref. [57]. Unlike the approach taken in our earlier work [22], we now perform fully correlated fits of the parameters, which leads to improved control over statistical uncertainties. Representative fits are shown in Fig. 4, with dashed lines indicating the region of data included in the fitting window. In all cases, we exclude points with $z \lesssim 0.6$ fm from the extrapolation procedure, as this distance appears sufficient for the onset of the expected exponential decay behavior. We include as many data points with reliable uncertainties as possible to ensure meaningful constraints on the fit parameters. As intended, the extrapolated form significantly constrains the large- $|z|$ tail of the matrix elements compared to lattice data alone.

We note that the treatment of the long-distance behavior and the associated systematic uncertainties remains a subject of active study [58–60]. Nevertheless, all fits yield χ^2/dof values consistent with unity, indicating that the adopted form provides an adequate description of the tail

region. Moreover, the contribution of this extrapolated part of the matrix elements to the intermediate- x region where LaMET predictions are most reliable is expected to be modest. A more comprehensive investigation of model and fit-range systematics will be pursued in future work.

The quasi-PDF is obtained by Fourier transforming the continuous matrix elements, which are constructed by combining the large- ν extrapolation with interpolations of the short-distance data. The resulting quasi-PDF is then matched to the corresponding light-cone PDF using the perturbative matching kernel of Ref. [22]. Quark mixing effects are neglected in this analysis. Representative results for both quasi-PDFs and their matched light-cone counterparts are shown in Fig. 5. In line with earlier studies of gluonic distributions within the LaMET framework [22], the quasi-PDFs typically display mild negative regions which are significantly reduced after applying the matching. Nevertheless, some residual negativity at large x persists in the matched PDFs, likely reflecting remaining lattice systematic effects, which we analyze in the following section.

With the extensive dataset available across multiple analyses, we can now explore the impact of various lattice systematics. Up to this point, our discussion has focused solely on statistical uncertainties, which are now relatively well controlled. The following results are therefore interpreted more qualitatively, acknowledging that systematic effects related to scale dependence and extrapolation may exceed the quoted statistical errors by several times. We begin by revisiting the smearing dependence to verify the trends observed at the level of the matrix elements. Figure 6 compares PDFs from different smearing analyses for several samples of lattice spacing, pion mass, and momentum. Overall, the PDFs are remarkably consistent across the different smearing schemes, with the three PDFs in each plot falling comfortably within 1σ from each other. This further demonstrates that self-renormalization is applicable to both the fixed-relative and fixed-physical smearing schemes, and removes any associated smearing effects. This suggests that taking the limit of zero flow time explicitly for the fixed-physical smearing scheme is not necessary; thus, we may move on to the other common systematics. In Fig. 7, we plot PDFs from fixed smearing scheme and pion mass, at nearly consistent momenta, across the three lattice spacings. As anticipated from the comparisons at the matrix-element level, lattice-spacing dependence is milder at the heavier pion mass (left column). Here, all lattice spacings yield results consistent within roughly 1σ across all smearing schemes. In contrast, the lighter pion mass (right column) exhibits more pronounced lattice-spacing effects, as expected. The results are consistent within $1\text{--}2\sigma$ across all lattice spacings; however, it is clear that a reduction in statistical error would likely increase the tension between results at different lattice spacings. One pleasing feature of the lattice-spacing effects is that smaller lattice spacings seem to lead to less negativity in the PDFs. This can be seen best in the top left and

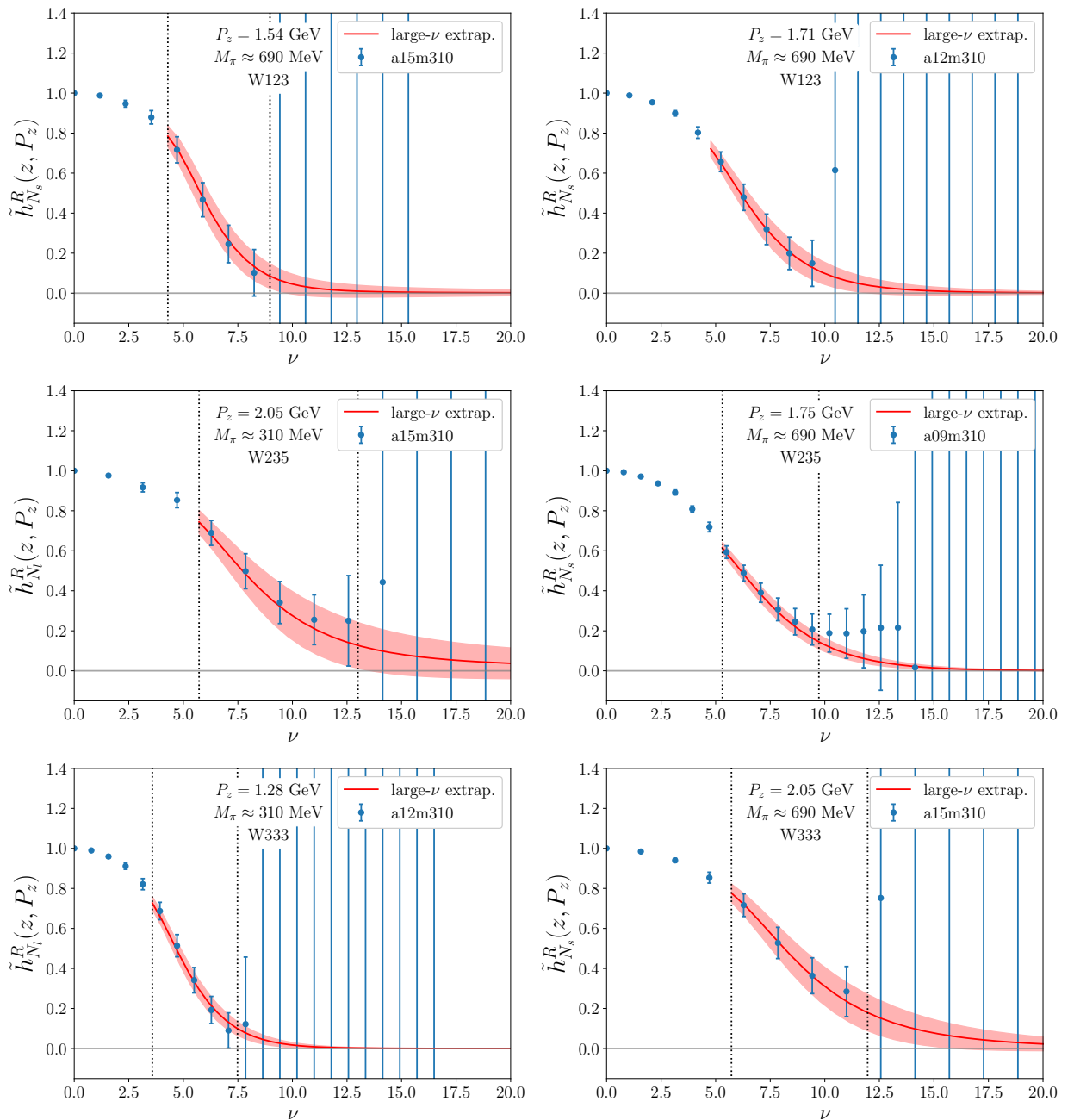


FIG. 4: Selected large- ν extrapolations at select momentum and ensemble for (top row) the W123 analysis, (middle row) the W235 analysis, and (bottom row) the W333 analysis. We use data from $z \gtrsim 0.6$ fm across all examples and the black dashed lines illustrate the range of z used in the fit

middle right figures. Some residual lattice-spacing dependence can be expected from the self-renormalization procedure, so finer lattice spacings and continuum extrapolations will be important for further controlling the lattice spacing effects, and reducing the unphysical negativity in the PDFs.

Now, we can move to the systematics which are not expected to be controlled by hybrid renormalization. In Fig. 8, we show the pion-mass dependence of a sample

of combinations of smearing analyses, momentum, and lattice spacing. We see good consistency between the two pion masses, with a maximum of 2σ differences in the center plot. This difference is not statistically significant, indicating that the pion-mass dependence is under control at the current level of precision. However, it would be valuable to confirm this in future work, either by performing a pion-mass extrapolation or by using improved algorithms and error reduction techniques that

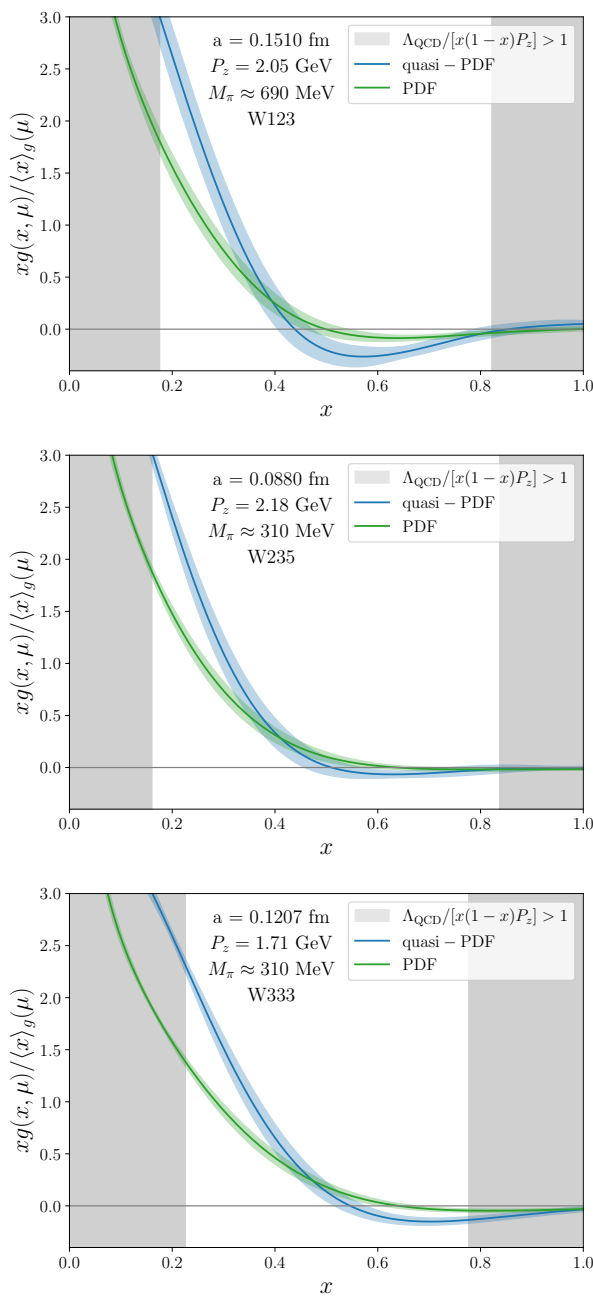


FIG. 5: A selection of quasi-PDFs and their corresponding lightcone PDFs after matching. From top to bottom, the lattice parameters correspond to $a \approx 0.15, 0.09, 0.12$ fm, $M_\pi \approx 690, 310$ MeV, $P_z = 2.05, 2.18, 1.71$ GeV, and smearing schemes W123, W235, and W333, respectively.

could make measurements at the physical pion mass more accessible. In particular, if the trend which is demonstrated most clearly in the center plot remains, physical pion mass may also contribute to a reduction in negativity of the PDF. Finally, in Fig. 9 we illustrate the momentum dependence of the PDFs for an arbitrary combination of lattice spacing, pion mass, and smearing choice; these plots are representative of the many other combi-

nations we have studied. Here, strong momentum dependence is observed across all smearing schemes, with deviations exceeding 3σ in most regions. This suggests that we may not have truly achieved the next-to-leading power accuracy in our LaMET expansion. This can be remedied by leading-renormalon resummation [61] and renormalization-group resummation [62], which have not yet been fully developed for the gluon. Perhaps the deviation could be controlled by an infinite-momentum extrapolation; however, one must consider that the infinite-momentum result would only be accurate in the region $\Lambda_{\text{QCD}} / (x(1-x)P_z^{\min}) < 1$. We wish to further control the systematic effects and increase the momentum further before we apply infinite-momentum extrapolations. We believe that pion mass and lattice-spacing effects are controllable via extrapolation at this point, but the momentum dependence is still quite large and needs to be understood further before an extrapolation is considered.

IV. CONCLUSIONS AND OUTLOOK

In this work, we systematically investigated lattice artifacts arising from variations in gauge-link smearing, lattice spacing, pion mass, and nucleon boost momentum in the self-renormalized nucleon gluon PDF determination using the LaMET method. We examined two smearing approaches, both using Wilson flow [46]: one with a fixed physical flow time and another with a fixed relative flow time on each ensemble. The results show no significant differences in the renormalized matrix elements or in the extracted PDFs between the two methods. Moreover, the dependence on the smearing level between different fixed physical flow times is negligible, suggesting that self-renormalization can control differences in smearing, and that extrapolation to zero flow time, is not even necessary. The applicability of self-renormalization to Wilson-flowed data is expected, as the linear divergence should be modified by a term proportional to $1/\sqrt{T_W} \propto 1/a$ [56]. In the case of fixed relative flow time, the self renormalization parameterization would be unchanged, while in the case of fixed physical flow time the modification of the linear divergence in fixed physical flow time can likely still be absorbed by the other terms in the self-renormalization parameterization. We found very small pion-mass dependence and mild lattice spacing in the final PDFs, no more than about 2σ . These could be controlled fully via extrapolations to the continuum-physical limit and constrained further by calculations at smaller lattice spacings and pion masses. On the other hand, we find strong momentum dependence, with differences corresponding to more than 3σ between the $P_z \approx 1.3$ and 2.2 GeV PDFs. These effects may be caused by lack of leading-renormalon resummation (LRR) [61] and renormalization-group resummation (RGR) [62], which have been developed for the flavor-nonsinglet parton distributions (see the recent review in Ref. [12] for example results), but are not yet available for the gluon PDF.

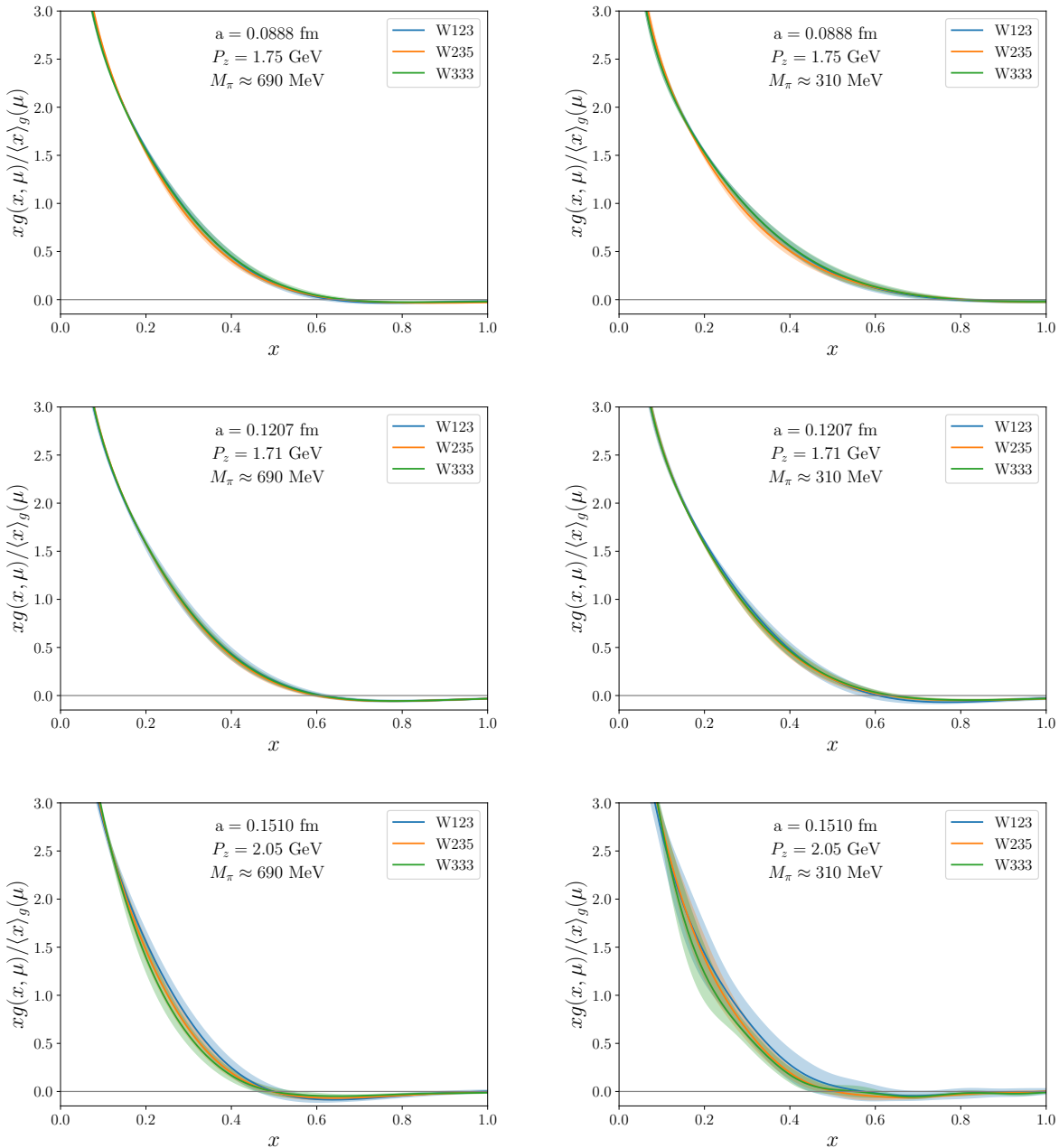


FIG. 6: Lightcone PDFs from the three smearing analyses for select momenta across the three lattice spacings, $a \approx 0.09$ (top row), 0.12 (middle row), and 0.15 (bottom row) fm and two pion masses, $M_\pi \approx 690$ (left column) and 310 MeV (right column).

These methods seem to improve momentum convergence in some of the leading twist-2 quark cases [63, 64], by taking care of the leading $\Lambda_{\text{QCD}}/2xP_z$ corrections; for our smallest-momentum PDFs which could be larger than 30% at $x = 0.5$ [61].

Future studies of the gluon PDF, supported by increased computational resources, can further reduce both statistical and systematic uncertainties. On the theoretical side, important questions remain regarding the optimal treatment of the Fourier transform in the quasi-PDF

reconstruction. Although higher boost momenta can in principle suppress leading LaMET systematics, achieving such boosts is difficult due to the rapidly deteriorating signal-to-noise ratio. To enable higher-momentum calculations, one promising direction is the use of recently proposed kinematically enhanced two-point operators, which exhibit significantly improved signal-to-noise behavior compared with traditional nucleon operators [42]. Once the perturbative matching is worked out, we can do a gauge fixed calculation of correlators without

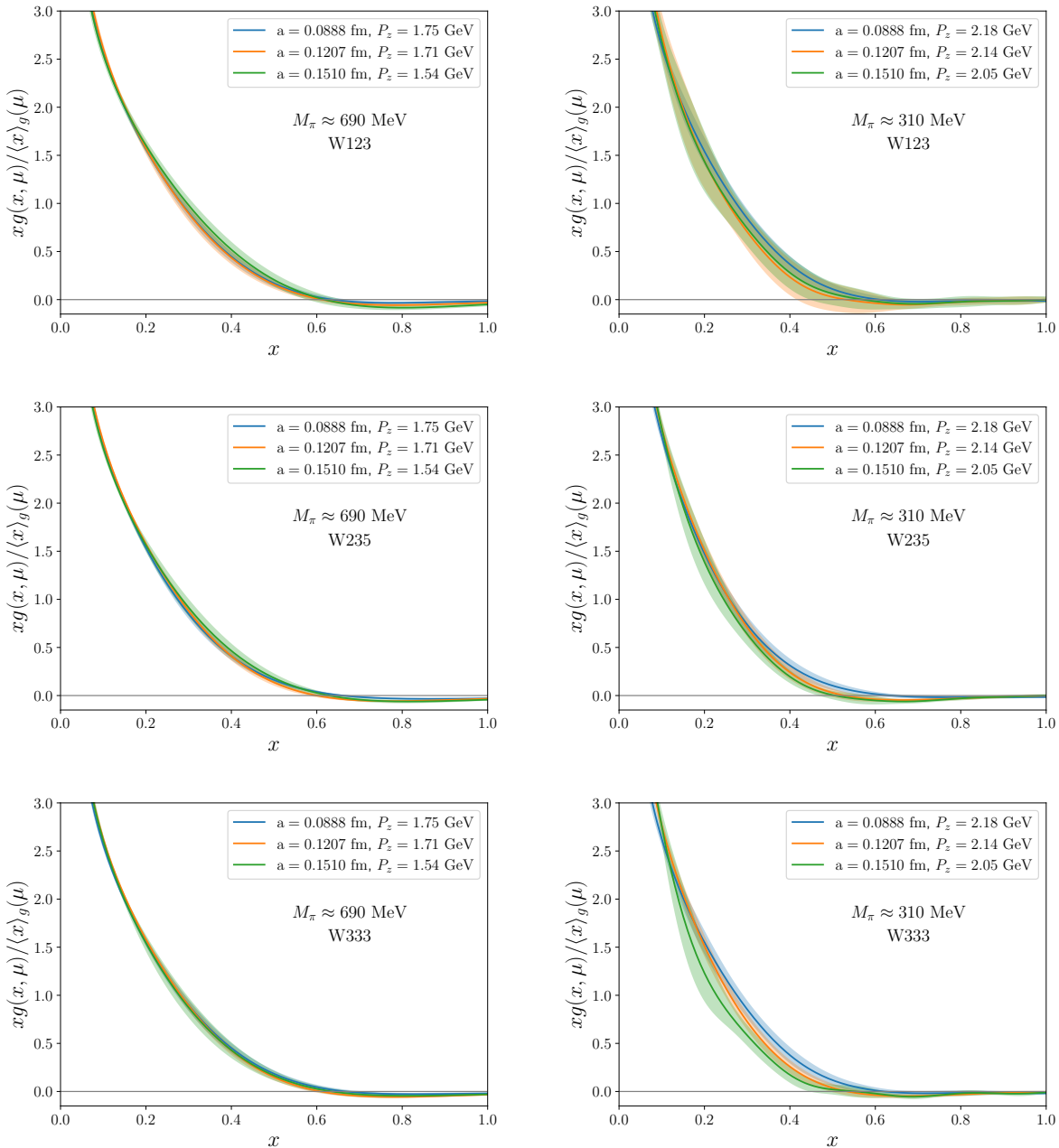


FIG. 7: Lightcone PDFs from the three smearing analyses W123 (top row), W235 (middle row), and W333 (bottom row) for select momenta across the three lattice spacings and two pion masses, $M_\pi \approx 690$ (left column) and 310 MeV (right column).

Wilson lines [21, 65] to significantly improve the signal at long distances and yield better control over the large- ν extrapolation; this may open the door to implementation of more sophisticated parametrizations of the extrapolation and exploration of Bayesian and machine-learning techniques [58, 66, 67] to reduce model dependence. Together with the finer lattice and lower pion masses, we can significantly improve the LaMET gluon PDFs from lattice QCD.

Acknowledgments

AN and WG thank Yong Zhao, Yushan Su, Joshua Lin for their valuable suggestions and feedback on the earlier self-renormalized gluon PDF results. We thank the MILC Collaboration for sharing the lattices used to perform this study. The LQCD calculations were performed using the Chroma software suite [68]. This research used resources of the National Energy Research Scientific Computing Center, a DOE Office of Science User Facility

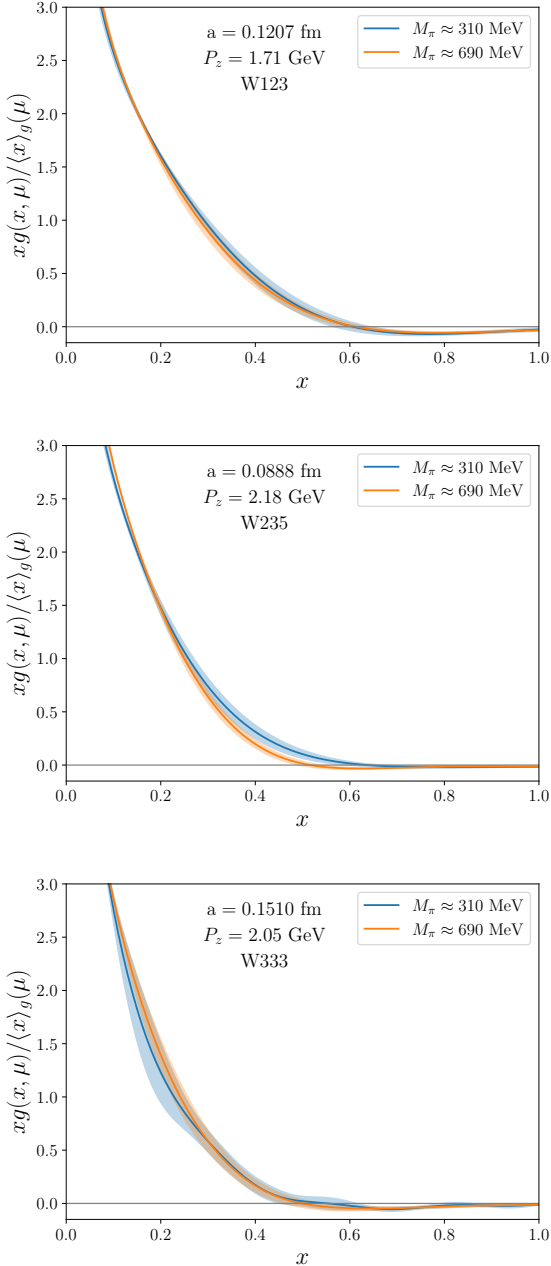


FIG. 8: Pion-mass dependence for a representative combination of smearing analyses, momentum, and lattice spacing. From top to bottom, the figures show $a \approx 0.12, 0.09, 0.15$ fm, $P_z \approx 1.71, 2.18, 2.05$ GeV, with W123, W235 and W333 smearing.

supported by the Office of Science of the U.S. Department of Energy under Contract No. DE-AC02-05CH11231 through ERCAP; facilities of the USQCD Collaboration, which are funded by the Office of Science of the U.S. Department of Energy, and supported in part by Michigan State University through computational resources provided by the Institute for Cyber-Enabled Research (iCER). The work of AN and WG is partially supported

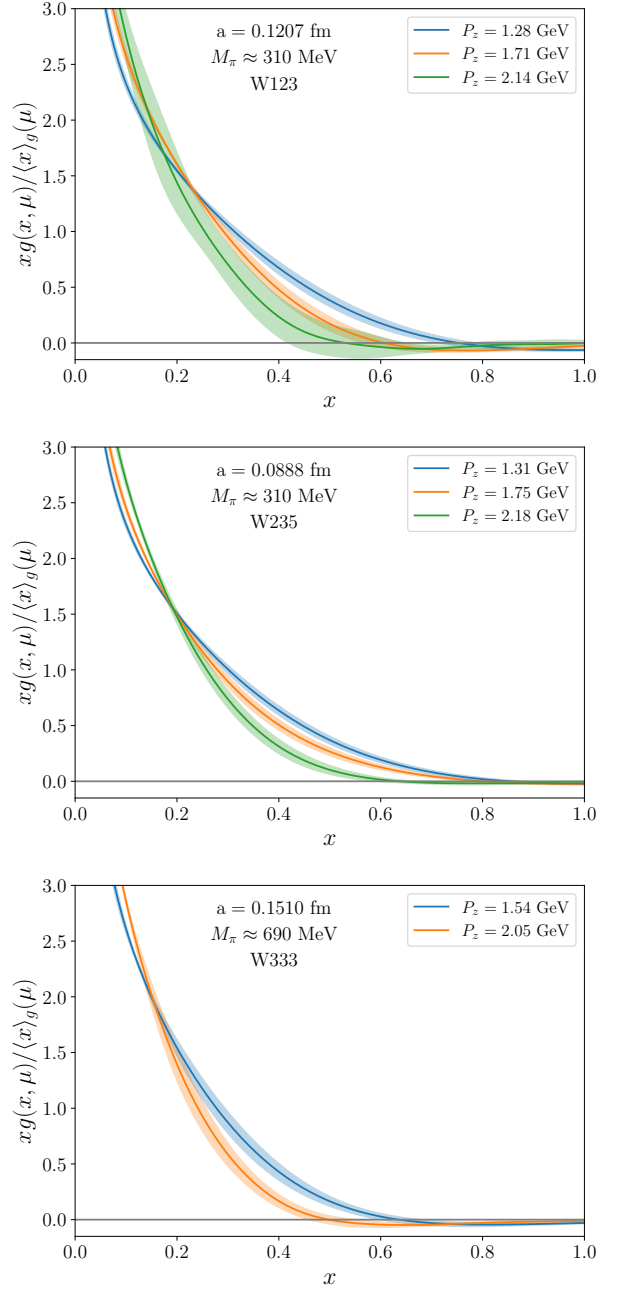


FIG. 9: Momentum dependence of the PDFs on a representative combination of lattice parameters. From top to bottom, the figures show $a \approx 0.12, 0.09, 0.15$ fm, $M_\pi \approx 310, 690$ MeV, with W123, W235 and W333 smearing.

by U.S. Department of Energy, Office of Science, under grant DE-SC0024053 “High Energy Physics Computing Traineeship for Lattice Gauge Theory”. The work of WG and HL is partially supported by the US National Science Foundation under grant PHY 2209424 and 2514533. FY is supported by the U.S. Department of Energy, Office of Science, Office of Nuclear Physics through Contract No. DE-SC0012704, and within the framework of Scientific Discovery through Advanced Computing (SciDAC)

[1] Tie-Jiun Hou et al. New CTEQ global analysis of quantum chromodynamics with high-precision data from the LHC. *Phys. Rev. D*, 103(1):014013, 2021.

[2] S. Amoroso et al. Snowmass 2021 Whitepaper: Proton Structure at the Precision Frontier. *Acta Phys. Polon. B*, 53(12):12-A1, 2022.

[3] P. Achenbach et al. The present and future of QCD. *Nucl. Phys. A*, 1047:122874, 2024.

[4] A. Accardi et al. Electron Ion Collider: The Next QCD Frontier: Understanding the glue that binds us all. *Eur. Phys. J. A*, 52(9):268, 2016.

[5] R. Abdul Khalek et al. Science Requirements and Detector Concepts for the Electron-Ion Collider: EIC Yellow Report. *Nucl. Phys. A*, 1026:122447, 2022.

[6] V. D. Burkert et al. Precision studies of QCD in the low energy domain of the EIC. *Prog. Part. Nucl. Phys.*, 131:104032, 2023.

[7] Xiangdong Ji. Parton Physics on a Euclidean Lattice. *Phys. Rev. Lett.*, 110:262002, 2013.

[8] Ian Balitsky, Wayne Morris, and Anatoly Radyushkin. Gluon Pseudo-Distributions at Short Distances: Forward Case. *Phys. Lett. B*, 808:135621, 2020.

[9] Xiangdong Ji, Yu-Sheng Liu, Yizhuang Liu, Jian-Hui Zhang, and Yong Zhao. Large-momentum effective theory. *Rev. Mod. Phys.*, 93(3):035005, 2021.

[10] Martha Constantinou et al. Parton distributions and lattice-QCD calculations: Toward 3D structure. *Prog. Part. Nucl. Phys.*, 121:103908, 2021.

[11] Huey-Wen Lin. Overview of Lattice Results for Hadron Structure. *Few Body Syst.*, 64(3):58, 2023.

[12] Huey-Wen Lin. Mapping parton distributions of hadrons with lattice QCD. *Prog. Part. Nucl. Phys.*, 144:104177, 2025.

[13] Zhouyou Fan, Rui Zhang, and Huey-Wen Lin. Nucleon gluon distribution function from 2 + 1 + 1-flavor lattice QCD. *Int. J. Mod. Phys. A*, 36(13):2150080, 2021.

[14] Zhouyou Fan, William Good, and Huey-Wen Lin. Gluon parton distribution of the nucleon from (2+1+1)-flavor lattice QCD in the physical-continuum limit. *Phys. Rev. D*, 108(1):014508, 2023.

[15] Tanjib Khan et al. Unpolarized gluon distribution in the nucleon from lattice quantum chromodynamics. *Phys. Rev. D*, 104(9):094516, 2021.

[16] Joseph Delmar, Constantia Alexandrou, Krzysztof Cichy, Martha Constantinou, and Kyriakos Hadjyiannakou. Gluon PDF of the proton using twisted mass fermions. *Phys. Rev. D*, 108(9):094515, 2023.

[17] Colin Egerer et al. Toward the determination of the gluon helicity distribution in the nucleon from lattice quantum chromodynamics. *Phys. Rev. D*, 106(9):094511, 2022.

[18] William Good, Kinza Hasan, Allison Chevis, and Huey-Wen Lin. Gluon moment and parton distribution function of the pion from $N_f=2+1+1$ lattice QCD. *Phys. Rev. D*, 109(11):114509, 2024.

[19] Alejandro Salas-Chavira, Zhouyou Fan, and Huey-Wen Lin. First glimpse into the kaon gluon parton distribution using lattice QCD. *Phys. Rev. D*, 106(9):094510, 2022.

[20] Alex NieMiera, William Good, and Huey-Wen Lin. Kaon gluon parton distribution and momentum fraction from 2+1+1 lattice QCD with high statistics. *Phys. Rev. D*, 112(7):074504, 2025.

[21] William Good, Kinza Hasan, and Huey-Wen Lin. Toward the first gluon parton distribution from the LaMET. *J. Phys. G*, 52(3):035105, 2025.

[22] William Good, Fei Yao, and Huey-Wen Lin. First Nucleon Gluon PDF from Large Momentum Effective Theory. 5 2025.

[23] Alex NieMiera, William Good, Huey-Wen Lin, and Fei Yao. First Self-Renormalized Gluon PDF of Nucleon from Large-Momentum Effective Theory in the Continuum Limit. 10 2025.

[24] Yi-Kai Huo et al. Self-renormalization of quasi-light-front correlators on the lattice. *Nucl. Phys. B*, 969:115443, 2021.

[25] Fei Yao et al. Nucleon Transversity Distribution in the Continuum and Physical Mass Limit from Lattice QCD. *Phys. Rev. Lett.*, 131(26):261901, 2023.

[26] Jun Hua et al. Pion and Kaon Distribution Amplitudes from Lattice QCD. *Phys. Rev. Lett.*, 129(13):132001, 2022.

[27] Jack Holligan, Xiangdong Ji, Huey-Wen Lin, Yushan Su, and Rui Zhang. Precision control in lattice calculation of x-dependent pion distribution amplitude. *Nucl. Phys. B*, 993:116282, 2023.

[28] Jack Holligan and Huey-Wen Lin. Nucleon helicity parton distribution function in the continuum limit with self-renormalization. *Phys. Lett. B*, 854:138731, 2024.

[29] A. Bazavov et al. Lattice QCD Ensembles with Four Flavors of Highly Improved Staggered Quarks. *Phys. Rev. D*, 87(5):054505, 2013.

[30] E. Follana, Q. Mason, C. Davies, K. Hornbostel, G. P. Lepage, J. Shigemitsu, H. Trottier, and K. Wong. Highly improved staggered quarks on the lattice, with applications to charm physics. *Phys. Rev. D*, 75:054502, 2007.

[31] Sungwoo Park, Rajan Gupta, Tanmoy Bhattacharya, Fangcheng He, Santanu Mondal, Huey-Wen Lin, and Boram Yoon. Flavor diagonal nucleon charges using clover fermions on MILC HISQ ensembles. *Phys. Rev. D*, 112(5):054508, 2025.

[32] Yong-Chull Jang, Rajan Gupta, Tanmoy Bhattacharya, Boram Yoon, and Huey-Wen Lin. Nucleon isovector axial form factors. *Phys. Rev. D*, 109(1):014503, 2024.

[33] Santanu Mondal, Rajan Gupta, Sungwoo Park, Boram Yoon, Tanmoy Bhattacharya, and Huey-Wen Lin. Moments of nucleon isovector structure functions in 2+1+1-flavor QCD. *Phys. Rev. D*, 102(5):054512, 2020.

[34] Yong-Chull Jang, Rajan Gupta, Huey-Wen Lin, Boram Yoon, and Tanmoy Bhattacharya. Nucleon electromagnetic form factors in the continuum limit from (2+1+1)-flavor lattice QCD. *Phys. Rev. D*, 101(1):014507, 2020.

[35] Rajan Gupta, Boram Yoon, Tanmoy Bhattacharya, Vincenzo Cirigliano, Yong-Chull Jang, and Huey-Wen Lin. Flavor diagonal tensor charges of the nucleon from (2+1+1)-flavor lattice QCD. *Phys. Rev. D*, 98(9):091501, 2018.

[36] Huey-Wen Lin, Rajan Gupta, Boram Yoon, Yong-Chull

Jang, and Tanmoy Bhattacharya. Quark contribution to the proton spin from 2+1+1-flavor lattice QCD. *Phys. Rev. D*, 98(9):094512, 2018.

[37] Rajan Gupta, Yong-Chull Jang, Boram Yoon, Huey-Wen Lin, Vincenzo Cirigliano, and Tanmoy Bhattacharya. Isovector Charges of the Nucleon from 2+1+1-flavor Lattice QCD. *Phys. Rev. D*, 98:034503, 2018.

[38] Tanmoy Bhattacharya, Vincenzo Cirigliano, Saul Cohen, Rajan Gupta, Anosh Joseph, Huey-Wen Lin, and Boram Yoon. Iso-vector and Iso-scalar Tensor Charges of the Nucleon from Lattice QCD. *Phys. Rev. D*, 92(9):094511, 2015.

[39] Tanmoy Bhattacharya, Vincenzo Cirigliano, Rajan Gupta, Huey-Wen Lin, and Boram Yoon. Neutron Electric Dipole Moment and Tensor Charges from Lattice QCD. *Phys. Rev. Lett.*, 115(21):212002, 2015.

[40] Tanmoy Bhattacharya, Saul D. Cohen, Rajan Gupta, Anosh Joseph, Huey-Wen Lin, and Boram Yoon. Nucleon Charges and Electromagnetic Form Factors from 2+1+1-Flavor Lattice QCD. *Phys. Rev. D*, 89(9):094502, 2014.

[41] Gunnar S. Bali, Bernhard Lang, Bernhard U. Musch, and Andreas Schäfer. Novel quark smearing for hadrons with high momenta in lattice QCD. *Phys. Rev. D*, 93(9):094515, 2016.

[42] Rui Zhang, Anthony V. Grebe, Daniel C. Hackett, Michael L. Wagman, and Yong Zhao. Kinematically enhanced interpolating operators for boosted hadrons. *Phys. Rev. D*, 112(5):L051502, 2025.

[43] Daniel C. Hackett, Dimitra A. Pefkou, and Phiala E. Shanahan. Gravitational Form Factors of the Proton from Lattice QCD. *Phys. Rev. Lett.*, 132(25):251904, 2024.

[44] Daniel C. Hackett, Patrick R. Oare, Dimitra A. Pefkou, and Phiala E. Shanahan. Gravitational form factors of the pion from lattice QCD. *Phys. Rev. D*, 108(11):114504, 2023.

[45] Yi-Kai Huo et al. Self-renormalization of quasi-light-front correlators on the lattice. *Nucl. Phys. B*, 969:115443, 2021.

[46] Martin Lüscher. Properties and uses of the Wilson flow in lattice QCD. *JHEP*, 08:071, 2010. [Erratum: JHEP 03, 092 (2014)].

[47] Jian-Hui Zhang, Xiangdong Ji, Andreas Schäfer, Wei Wang, and Shuai Zhao. Accessing Gluon Parton Distributions in Large Momentum Effective Theory. *Phys. Rev. Lett.*, 122(14):142001, 2019.

[48] Jiunn-Wei Chen, Xiangdong Ji, and Jian-Hui Zhang. Improved quasi parton distribution through Wilson line renormalization. *Nucl. Phys. B*, 915:1–9, 2017.

[49] Taku Izubuchi, Xiangdong Ji, Luchang Jin, Iain W. Stewart, and Yong Zhao. Factorization Theorem Relating Euclidean and Light-Cone Parton Distributions. *Phys. Rev. D*, 98(5):056004, 2018.

[50] Constantia Alexandrou, Krzysztof Cichy, Martha Constantinou, Kyriakos Hadjijyannakou, Karl Jansen, Haralampos Panagopoulos, and Fernanda Steffens. A complete non-perturbative renormalization prescription for quasi-PDFs. *Nucl. Phys. B*, 923:394–415, 2017.

[51] Anatoly Radyushkin. One-loop evolution of parton pseudo-distribution functions on the lattice. *Phys. Rev. D*, 98(1):014019, 2018.

[52] Vladimir M. Braun, Alexey Vladimirov, and Jian-Hui Zhang. Power corrections and renormalons in parton quasidistributions. *Phys. Rev. D*, 99(1):014013, 2019.

[53] Zheng-Yang Li, Yan-Qing Ma, and Jian-Wei Qiu. Multiplicative Renormalizability of Operators defining Quasi-parton Distributions. *Phys. Rev. Lett.*, 122(6):062002, 2019.

[54] Xiangdong Ji, Yizhuang Liu, Andreas Schäfer, Wei Wang, Yi-Bo Yang, Jian-Hui Zhang, and Yong Zhao. A Hybrid Renormalization Scheme for Quasi Light-Front Correlations in Large-Momentum Effective Theory. *Nucl. Phys. B*, 964:115311, 2021.

[55] Chen Chen, Yiqi Geng, Liuming Liu, Peng Sun, Yi-Bo Yang, Fei Yao, Jian-Hui Zhang, and Kuan Zhang. Parton distribution function of a deuteronlike dibaryon system from lattice QCD. *Phys. Rev. D*, 111(7):074506, 2025.

[56] Nora Brambilla and Xiang-Peng Wang. Off-lightcone Wilson-line operators in gradient flow. *JHEP*, 06:210, 2024.

[57] Xiang Gao, Andrew D. Hanlon, Swagato Mukherjee, Peter Petreczky, Philipp Scior, Sergey Syritsyn, and Yong Zhao. Lattice QCD Determination of the Bjorken-x Dependence of Parton Distribution Functions at Next-to-Next-to-Leading Order. *Phys. Rev. Lett.*, 128(14):142003, 2022.

[58] Hervé Dutrieux, Joe Karpie, Christopher J. Monahan, Kostas Orginos, Anatoly Radyushkin, David Richards, and Savvas Zafeiropoulos. Inverse problem in the LaMET framework. 4 2025.

[59] Jiunn-Wei Chen et al. LaMET’s Asymptotic Extrapolation vs. Inverse Problem. 5 2025.

[60] Hervé Dutrieux, Joe Karpie, Christopher J. Monahan, Kostas Orginos, Anatoly Radyushkin, David Richards, and Savvas Zafeiropoulos. Comment on ”LaMET’s Asymptotic Extrapolation vs. Inverse Problem”. 6 2025.

[61] Rui Zhang, Jack Holligan, Xiangdong Ji, and Yushan Su. Leading power accuracy in lattice calculations of parton distributions. *Phys. Lett. B*, 844:138081, 2023.

[62] Yushan Su, Jack Holligan, Xiangdong Ji, Fei Yao, Jian-Hui Zhang, and Rui Zhang. Resumming quark’s longitudinal momentum logarithms in LaMET expansion of lattice PDFs. *Nucl. Phys. B*, 991:116201, 2023.

[63] Xiang Gao, Andrew D. Hanlon, Swagato Mukherjee, Peter Petreczky, Qi Shi, Sergey Syritsyn, and Yong Zhao. Transversity PDFs of the proton from lattice QCD with physical quark masses. *Phys. Rev. D*, 109(5):054506, 2024.

[64] Heng-Tong Ding, Xiang Gao, Swagato Mukherjee, Peter Petreczky, Qi Shi, Sergey Syritsyn, and Yong Zhao. Three-dimensional imaging of pion using lattice QCD: generalized parton distributions. *JHEP*, 02:056, 2025.

[65] Xiang Gao, Wei-Yang Liu, and Yong Zhao. Parton distributions from boosted fields in the Coulomb gauge. *Phys. Rev. D*, 109(9):094506, 2024.

[66] Talal Ahmed Chowdhury, Taku Izubuchi, Methun Kamruzzaman, Nikhil Karthik, Tanjib Khan, Tianbo Liu, Arpon Paul, Jakob Schoenleber, and Raza Sabbir Sufian. Polarized and unpolarized gluon PDFs: Generative machine learning applications for lattice QCD matrix elements at short distance and large momentum. *Phys. Rev. D*, 111(7):074509, 2025.

[67] Hervé Dutrieux, Joseph Karpie, Kostas Orginos, and Savvas Zafeiropoulos. Simple nonparametric reconstruction of parton distributions from limited Fourier information. *Phys. Rev. D*, 111(3):034515, 2025.

[68] Robert G. Edwards and Balint Joo. The Chroma soft-

ware system for lattice QCD. *Nucl. Phys. B Proc. Suppl.*, 140:832, 2005.